

## ADVANCED MODELING OF BUCKLING DELAYED SHEAR LINKS UNDER STRONG CYCLIC LOADS

J. Ramirez M.<sup>1 2</sup>, G. Bozzo<sup>2 3</sup>, J. M. Gonzalez<sup>1 2</sup>, F. Rastellini<sup>1 2</sup>, J. Irazabal<sup>1</sup>, L. Bozzo<sup>3 4</sup>

<sup>1</sup>Centre Internacional en Metodes Numerics a l'Enginyeria (CIMNE). Barcelona, Spain  
{jramirez, frastellini, jirazabal}@cimne.upc.edu

<sup>2</sup>Universitat Politècnica de Catalunya (UPC). Barcelona, Spain  
jose.manuel.gonzalez@upc.edu

<sup>3</sup>SLB Devices. Barcelona, Spain  
info@slbdevices.com

<sup>4</sup>Luis Bozzo Estructuras y Proyectos S. L. Barcelona, Spain  
lbozrot@ciccp.es

---

### Abstract

*This study investigates the advanced numerical modelling of a Buckling Delayed Shear Link (BDSL) system as a response control device aimed at improving the seismic resilience of structures. This system combines shear-based dissipative devices with an improved connection that transmits shear loads while preventing axial force, allowing for in-plane rotation. It currently accommodates displacements up to 60 mm. Experimental tests using cyclic loading were performed on specific dissipative element geometry to calibrate the mechanical properties and validate the numerical model. The tests, performed at the structures laboratory of the University of Lima, Peru, adhered to cyclic loading protocols following standard codes. The tests provided the structural response of the system in terms of hysteretic curves and failure modes. The methodology focuses on creating a three-dimensional numerical model of the BDSL using the Finite Element Method (FEM) to simulate its behaviour under cyclic loads. The FEM model of the dissipator features large displacements and incorporates both material and contact nonlinearities. ASTM A36 steel has been evaluated using a combined hardening model to represent its cyclic behaviour. A penalty-based algorithm handles contact in the special connection, ensuring accurate seismic response. The results show strong agreement regarding displacements, total shear forces, hysteretic curves, dissipated energy, and effective stiffness. Additionally, the experimental failure mode is analysed by considering key numerical variables: equivalent plastic strain and stress triaxiality. The analysis of key variables from calibrated models and numerical simulation data will be used to train a surrogate model using machine learning techniques. With this approach, the system can be optimised, and the structural response can be predicted at a low computational cost.*

**Keywords:** Buckling Delayed Shear Link, Finite Element Method, Seismic energy dissipation, Cyclic behavior, Numerical modeling, Machine Learning-based optimization

---

## 1 INTRODUCTION

Since the 1980s, the implementation of seismic protection technologies in structural design has been increasingly significant [1]. In contrast to traditional seismic design that relies on structural redundancy, these methods provide more efficient material distribution, improved earthquake performance, and simplified post-earthquake inspection and repair. They function as response control systems that enhance structural resilience.

Soong and Spencer classified supplemental energy dissipation devices into base isolation, passive energy dissipation, and active control systems [2]. Base isolation is mostly effective for low-to mid-rise buildings, as it decouples the superstructure from the ground, making it inadequate for high structures. Although it significantly reduces seismic forces, it involves considerable costs and complexity, and any failure or obstruction of the system could lead to the collapse of the entire structure.

Symans et al. summarised current applications and recent developments in passive energy dissipation systems, including the mechanical behaviour, mathematical models, and design methodologies of common devices, such as viscous fluids and viscoelastic, metallic, and friction dampers [3].

In this context, the present research focuses on the advanced numerical modelling of a specific passive seismic protection system: the Buckling Delayed Shear Link (BDSL). The objective is to develop a robust numerical model of the BDSL, validated through an experimental campaign of cyclic tests. This process will enable the study of its behaviour up to failure and support the development of a machine learning model for predicting structural responses.

## 2 BUCKLING DELAYED SHEAR LINK (BDSL) SYSTEM

The BDSL system, also known as the Shear Link Bozzo, is based on the same operational principle as the dissipative structural system for eccentrically braced frames developed by Popov and Engelhardt [4].

SLB seismic energy dissipators are devices that operate through metal yielding. Due to their substantial stiffness, they enable the development of rigid and ductile structures that are capable of withstanding severe seismic events with minimal structural damage.

Due to the more effective energy dissipation capabilities of steel, particularly under shear stresses, these devices have been employed in both masonry walls and reinforced concrete buildings. They depend on the capacity of the metal to absorb energy through plastic deformation caused by shear forces. The SLB device incorporates a steel component with a localised thickness reduction at the web, accomplished through milling, resulting in thinner areas referred to as "dissipative windows".

SLB dissipators emerged in the early 2000s, initially designed for masonry walls. Hurtado and Bozzo presented numerical and experimental results of a preliminary set of SLB devices, demonstrating their effectiveness in energy dissipation [5]. The first two generations featured bolted connections at both ends, resulting in fully restrained boundary conditions.

Nuzzo documented the experimental campaign of the third generation of SLB devices, conducted at the University of Naples Federico II, Italy [6]. This version introduced a battlement connection, which replaced the previous double-fixed condition with a fixed-pinned boundary configuration. This change improved structural performance and adaptability, allowing deformations of up to 3 cm.

Subsequently, a fourth generation was developed, achieving deformations up to 5 cm and further enhancing ductility and energy dissipation capacity [7]. This version retained the

special connection and introduced refinements that allowed even greater deformation capacity.

Figure 1 illustrates the BDSL system, which corresponds to the fourth generation of SLB devices [8]. This line of research has led to the development of a refined version of fourth-generation devices capable of reaching deformations up to 6 cm. Figure 1a shows the placement of the BDSL system within structural walls; Figure 1b presents its detailed configuration, and Figure 1c displays the full-scale physical model.

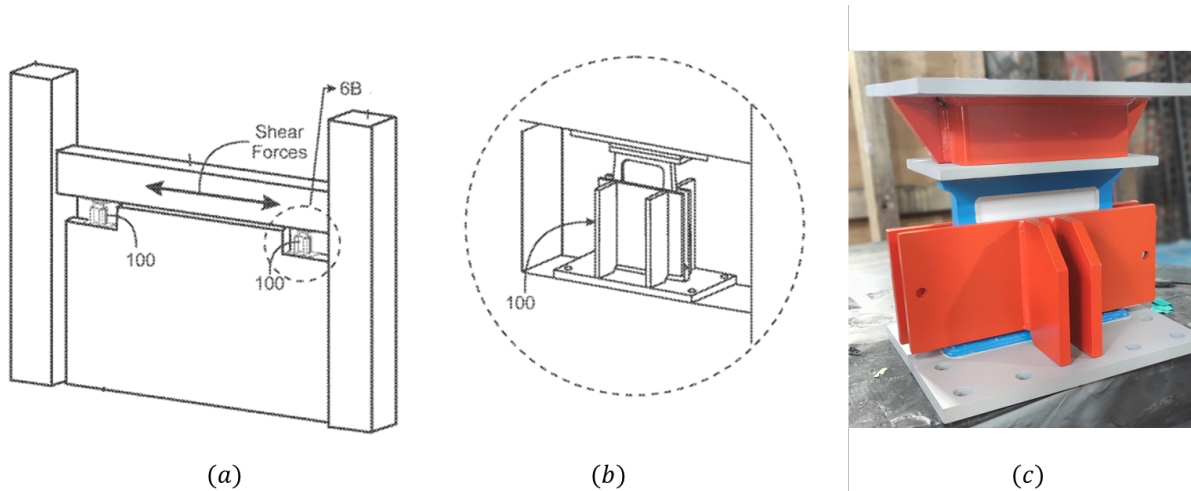


Figure 1. (a) Schematic of shear wall test setup with BDSL device; (b) detail of the dissipator location within the structure; (c) physical model of the BDSL energy dissipation device

The SLB dissipators and the BDSL system have been tested in several countries, including Italy, Portugal, Spain, and Peru. Their application has primarily focused on new constructions and the retrofitting of existing buildings.

These energy dissipators represent an attractive alternative for medium-to high-rise buildings. In particular, BDSL dissipators offer a wide range of applications thanks to their mechanical properties, especially their high stiffness and the absence of axial load transmission.

However, research also supports their implementation in other structures, such as wind towers, precast buildings [9-11], and tall bridges [12]. Notably, BDSL dissipators have been incorporated into Landmark projects such as the Paradox Tower and the Oak 58 Tower in Mexico, both of which exceed 200 metres in height and have more than 60 stories.

SLB devices are generally made of steel, an isotropic material that is relatively easy to describe. However, the geometric complexity of the devices and the large deformations they must withstand make accurate numerical modelling highly challenging.

Although the material itself is well understood, the global mechanical response of the system is strongly influenced by geometric variability, which introduces uncertainty—especially under large deformations where second-order effects become relevant. Moreover, their high stiffness complicates experimental testing, as an extremely rigid auxiliary structure is required to ensure proper boundary conditions, along with a hydraulic press capable of applying the high forces involved.

In this context, numerical simulations play a key role in reducing uncertainty, supporting the selection and refinement of prototypes, and predicting their structural behaviour prior to physical testing.

### 3 EXPERIMENTAL TESTING

This study utilised tests from the University of Lima laboratory in Peru, equipped with a  $\pm 1000$  kN (compression/tension) hydraulic press and a 6-metre-high reaction wall for applying shear loading to the cantilevered device. The setup is optimised for both stability and stiffness. The design of this setup optimally balances simplicity and rigidity, ensuring the accurate characterisation of BDSL dissipators [13].

Its auxiliary structure ensures in-plane free deformation and lateral stability while remaining within the elastic range. Five LVDTs were used to measure displacements during the tests: three for the tested device (two capture vertical motion and one measure horizontal displacement) and two for the auxiliary structure. This setup enabled precise motion tracking, verification of boundary conditions, and evaluation of the mechanical behaviour of the devices under applied loads. Since 2022, this configuration has enabled several mechanical tests, reaching displacements up to 80 mm and loads up to 700 kN [14].

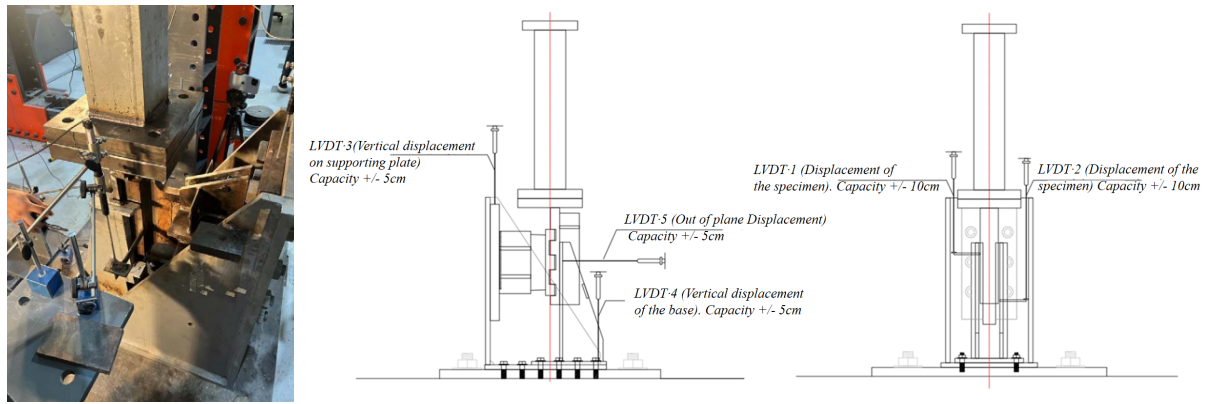


Figure 2. Instrumentation Set-up: Lateral and Frontal View of LVDT Configuration

The energy-dissipating piece of the BDSL dissipator consists of two distinct components: a frame with uniform thickness and windows with variable geometric configurations. The prototype selected for this study corresponds to the commercial nomenclature BDSL 4\_25\_8, with a height of 30 mm, a window thickness of 8 mm, and a frame thickness of 25 mm. These dimensions are illustrated in Figure 3.

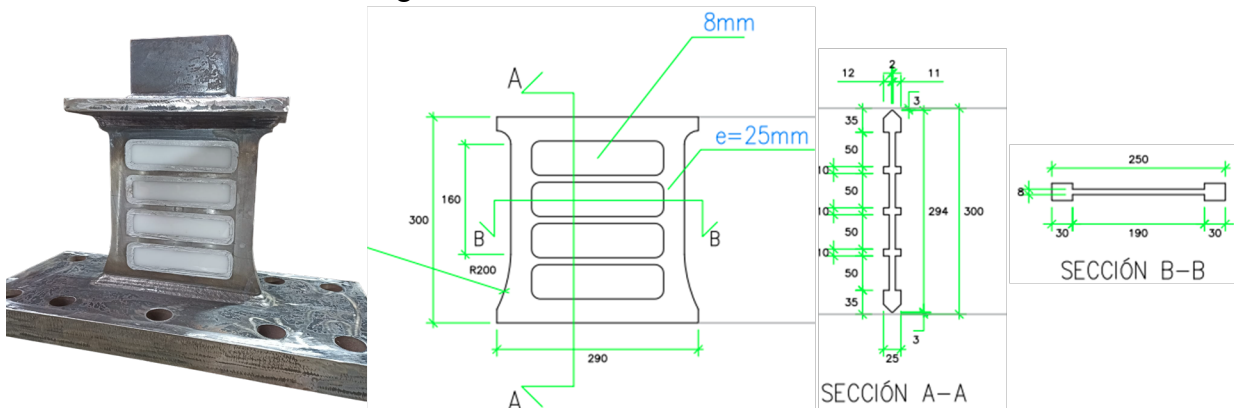


Figure 3. Geometry and Instrumentation of the BDSL Specimen: Frontal, Lateral, and Cross-Section Views

The experimental tests follow ANSI/AISC 341-16 [15] and ASCE 7-22 [16] standards. These codes specify the test design, verification of auxiliary elements, and loading protocols. Three distinct loading patterns were defined to evaluate the dissipation system, as illustrated



in Figure 4. Each loading pattern includes a different number of cycles, with amplitudes of 16 mm, 32 mm, 48 mm, 64 mm, and 80 mm. Additionally, the figure indicates the failure point for each test.

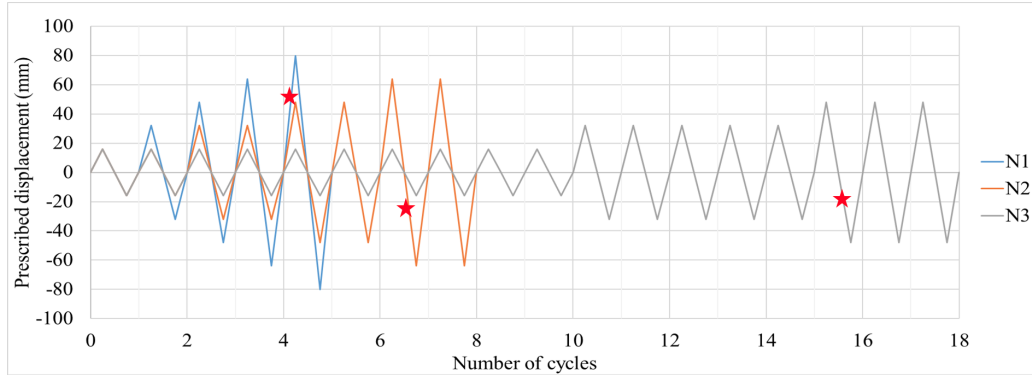


Figure 4. Loading patterns

The structural response of the studied dissipator is represented by its hysteresis curve, showing failure points at different positions (Figure 5). Figure 6 illustrates the failure mode observed in a dissipator from test N3. The failure mode of the BDSL dissipative frame depends on the amplitude and number of deformation cycles applied.

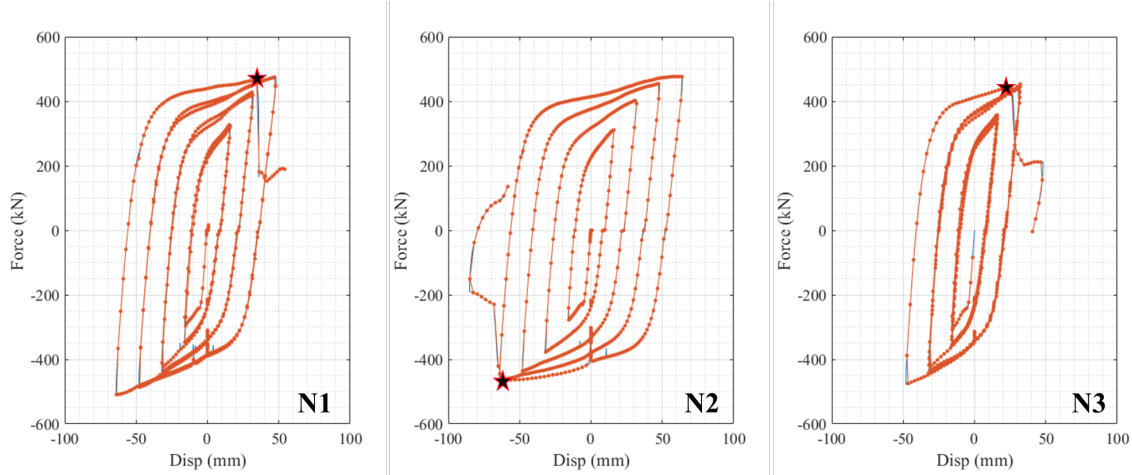


Figure 5. Hysteretic curves for experimental tests N1, N2, and N3

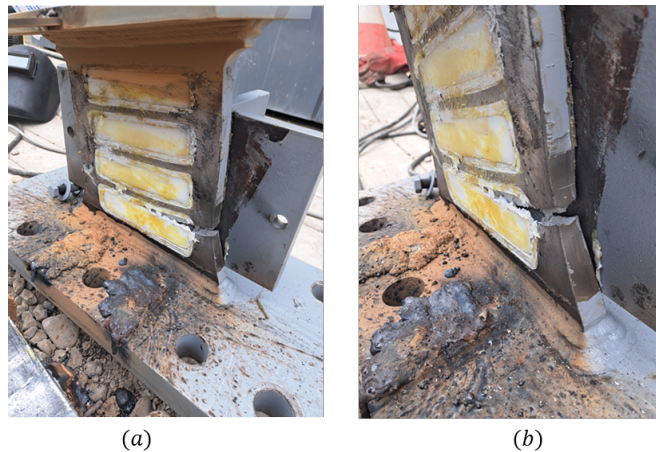


Figure 6. a) Front view of failure mode; b) Side view of frame failure mode in the BDSL system during test N3.

## 4 NUMERICAL MODELING OF THE BDSL SYSTEM

This section presents the finite-element model developed to simulate the behaviour of the BDSL system. The modelling assumptions—geometry, material properties, boundary conditions, and contact algorithms—are described in detail. Calibration procedures are also included to ensure an accurate representation of the system response under cyclic loading, serving as a basis for subsequent validation against experimental data.

### 4.1 Numerical Modeling of the BDSL Dissipation System

The numerical models were developed using the COMPACK code. This code was created by the International Centre for Numerical Methods in Engineering (CIMNE) for explicit dynamic analyses. The finite element method (FEM) is used by COMPACK, and it works by simulating dynamic analyses of composite structures using an incremental explicit approach [17–18].

The physical configuration of the BDSL system is shown in Figure 7a, providing an overview of its structural components. Figure 7b displays the numerical model developed for simulation purposes. The dissipative elements feature a variable and symmetric geometry, clearly illustrated in Figure 7c.

The BDSL system features a rigid frame designed according to specific parameters. It incorporates dissipative windows with rounded edges, which are automatically machined with reduced thicknesses to enhance their performance under cyclic loading. The boundary conditions include an upper connection formed by rigid components, separated by a 0.5 mm gap, which prevents the transmission of axial forces. This connection is modelled using structured meshes composed of regular triangular elements (see Figure 7d).

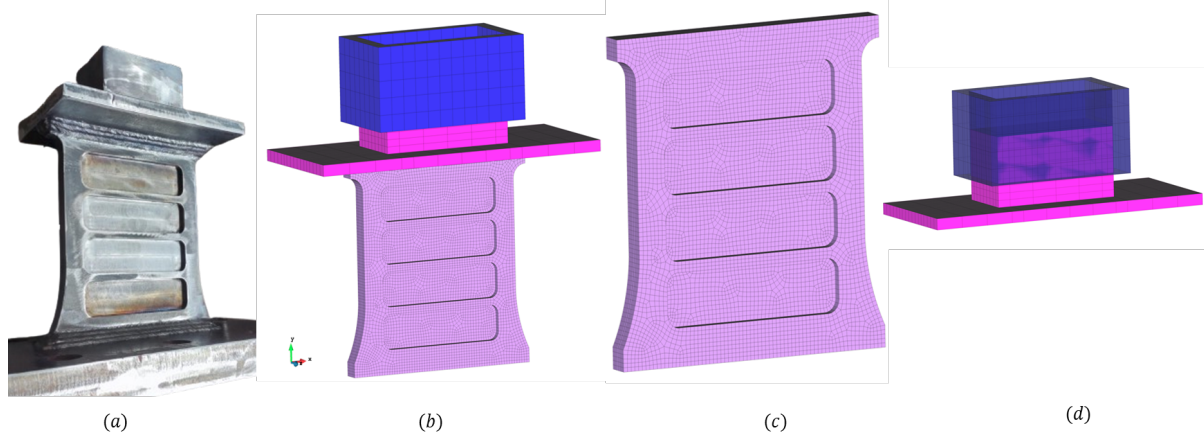


Figure 7. a) Geometry of the BDSL system; b) Finite element model of the BDSL system; c) Mesh discretisation of the BDSL device; d) Mesh discretisation of the upper connection.

The numerical model was developed using a structured discretisation with linear isoparametric 8-node hexahedral solid elements in three dimensions. Gauss point integration schemes were applied to ensure accurate representation of shear behaviour and uniform volumetric deformation. Geometric nonlinearities were taken into account through the Total Lagrangian formulation, which is based on the additive decomposition of the logarithmic strain tensor. This methodology is particularly well-suited for capturing large inelastic deformations with high fidelity [19].

## 4.2 Nonlinear Behaviour of BDSL System

### 4.2.1. Material Properties (ASTM A36 Steel)

To accurately simulate the response of ASTM A36 steel under seismic loading, this study calibrates the mechanical properties of the material used in the dissipative components of the BDSL system. The cyclic response and plastic deformation of the material during seismic events are captured by a combined hardening model of isotropic and kinematic components. The nonlinear behaviour of steel under realistic loading conditions is accurately represented by experimental calibration.

Advances in computational mechanics have introduced more sophisticated plasticity models, such as the Yoshida-Uemori (Y-U) isotropic-kinematic hardening model. This model has proven highly effective in capturing the cyclic behaviour of steel and other metals, particularly under large deformation conditions [20-22].

Notably, the Y-U constitutive model can accurately capture complex material phenomena like the transient Bauschinger effect, permanent softening, and hardening stagnation under large elasto-plastic deformations. In order to accurately simulate energy dissipation devices such as the BDSL system, the Y-U model provides a more accurate description of kinematic hardening behaviour than traditional constitutive theories.

The numerical model is carefully calibrated using parameters adjusted from experiments conducted by Jia [23], see Table 1. ASTM A36 steel has a density of  $\rho = 7800 \text{ kg/m}^3$ , an elastic modulus of  $E_o = 200 \text{ GPa}$ , and a Poisson's ratio  $\mu = 0.30$ .

Plasticity parameters							Parameters for prestrain-dependent Young's moduli		
Y	b	C	m	B	Rsat	h	Eo	Ea	$\xi$
255.9	194.9	338.7	7.9	277.3	196.0	0.50	200	152	30.8

Table 1. Material parameters in the Y-U model. (Y, b, B, Rsat in MPa; Eo and Ea in GPa)

The suitability of the Yoshida-Uemori model for seismic device studies is finally validated by numerical results obtained with these parameters, as shown in Figure 6. These findings indicate that the model accurately simulates the behaviour of ASTM A36 steel under complex cyclic histories (KA03-KA07) and monotonic loading (KA01).

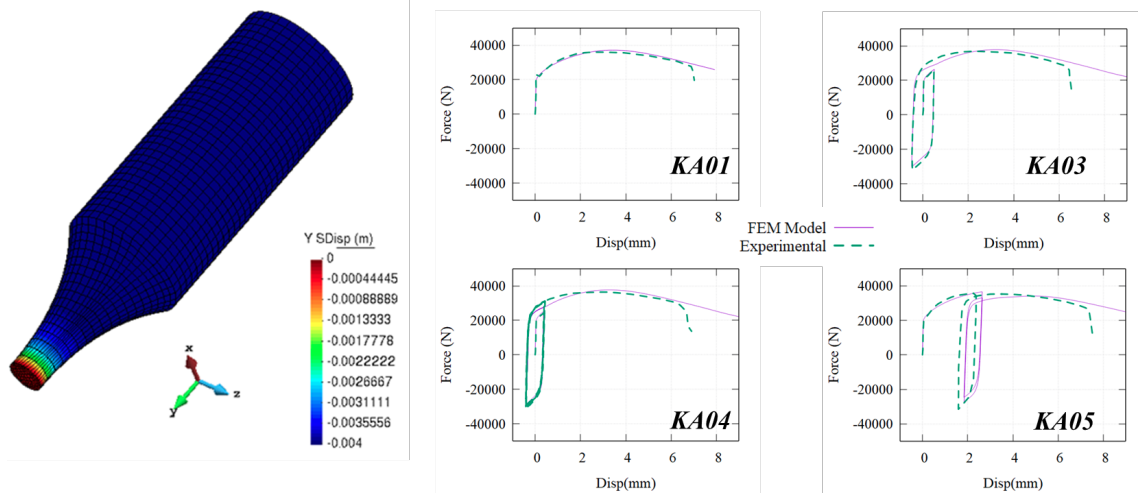


Figure 6. FEM Simulation of ASTM A36 steel under Monotonic and Cyclic Loadings

#### 4.2.2. Contact Mechanics and the Penalty-Based Algorithm

Compack software applies a three-dimensional penalty-based algorithm to model this contact behaviour [24-26]. The algorithm was initially developed for large deformation analysis in sheet stamping processes. It employs explicit integration and interpolates contact surfaces using triangular or quadrilateral segments. In this study, frictional effects between the connection components are not considered.

Figure 7 illustrates the mechanical contact surfaces in the BDSL system. The upper and lower connections are represented as rigid bodies. Contact occurs at two key areas: the upper and lower contact surfaces. These surfaces control the interaction between the connection pieces and the BDSL device. The contact is defined to prevent axial force transmission and allow sliding. This sliding is important for the energy dissipation mechanism. The BDSL device is placed at the bottom and deforms under cyclic loading. Contact forces at the BDSL system connection will be extracted from the FEM model to assess the response of the system numerically.

Figure 8 highlights the key mechanical components of the BDSL system. The assembly consists of a flexible actuator at the top, which connects to the upper structural component. A bottom piece links the actuator to the main BDSL frame. This frame is specifically designed to resist buckling during cyclic loading. A flexible base is included at the bottom to reproduce realistic boundary conditions. Within the frame, a local buckling control plane directs deformation into the four dissipative windows, ensuring that energy is absorbed efficiently in the intended regions. To simulate this behaviour, two pairs of contact interfaces are defined between the dissipative element and the rigid planes responsible for controlling its deformation.

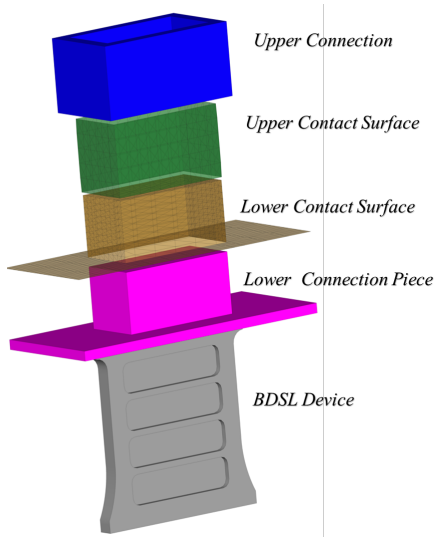


Figure 7. Mechanical contact surfaces in the BDSL system

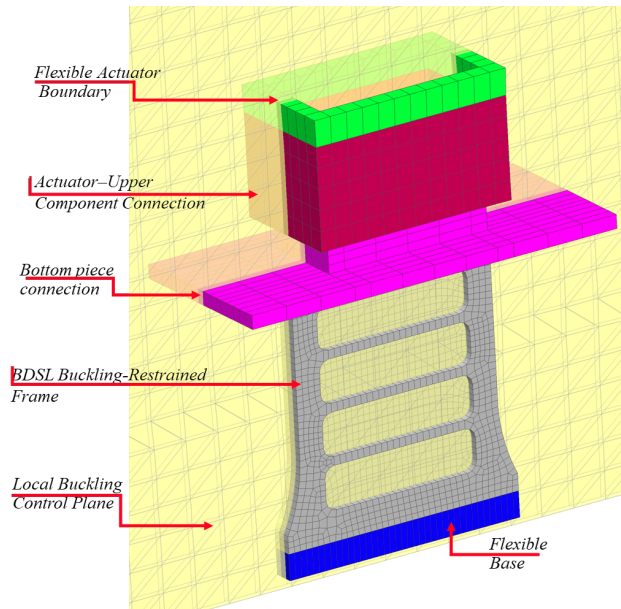


Figure 8. Mechanical configuration of the BDSL system

#### 4.3 Boundary and Kinematic Conditions

The finite element models incorporate customised boundary and kinematic conditions to represent the system response under the defined test parameters accurately. Figure 9a illustrates the implementation of these conditions in the BDSL system.

A prescribed displacement is applied at the top of the model, simulating the action of a flexible actuator. This load is transmitted through the upper connection, while the lower connection links the actuator to the BDSL device. The dissipative component, composed of a steel frame with four openings, is the primary region where deformation is concentrated. A fixed plane is defined at the base, fully constraining displacements and representing the system support. To ensure connection rigidity, the master-slave condition is applied at both ends of the device by linking secondary nodes to reference nodes.

Figure 9b shows the definition of the buckling control planes: one located at the interface between the BDSL device and the actuator and another at the lower zone of the frame. These planes are intended to guide deformation toward specific regions, providing control over the structural response under cyclic loading.

At first, a rigid base was thought of, but later, elastic hexahedral solid elements were added below the dissipative parts to better show how flexible the physical system is. This adjustment improved the global response and resulted in a lower stiffness slope in the hysteretic curve. These modelling strategies define the adopted methodology and allow for the simulation of energy dissipation mechanisms that are consistent with those observed in quasi-static experimental testing.

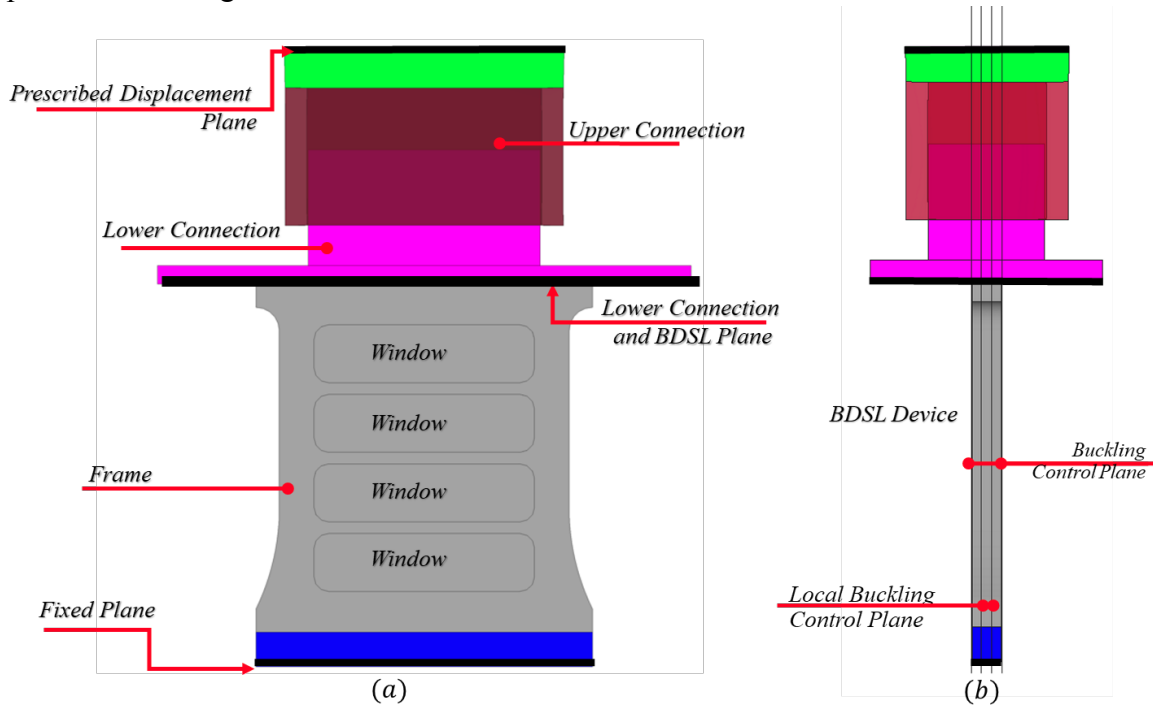


Figure 9. (a) Boundary and Kinematic Conditions; (b) Global and Local Buckling Control Planes

#### 4.4 Triaxiality Failure Diagram (TFD)

A Triaxiality Failure Diagram (TFD) is presented as a three-dimensional failure criterion with clearly defined safety zones. It was created using the Compack solver [27]. This diagram establishes a direct relationship between equivalent plastic strain at failure and stress triaxiality. Its stress-based formulation is particularly advantageous for accurate numerical prediction of material failure.

The simulations defined for ASTM A36 steel assign a triaxial failure curve. The plastic strains at fracture and stress triaxiality were looked at along with the equivalent plastic strain, as shown in Figure 10 from studies by Zhuang [28].



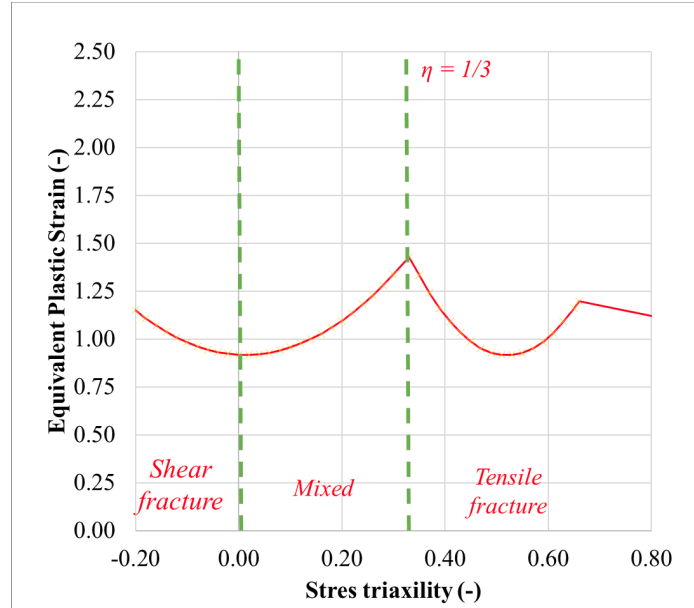


Figure 10. Triaxiality Failure Curve (TFC) for ASTM A36 steel.

#### 4.5 Validation of Boundary Conditions

Figure 11 shows the hysteresis curves from test N2 and the Finite Element Method (FEM) model of the BDSL damper that is fixed to a rigid base. The material behaviour is defined using the Y–U model parameters listed in Table 1. To ensure a consistent comparison, the analysis includes the response up to the failure point. Some discrepancies are observed in the unloading branches and near the failure region (marked red), where the experimental specimen exhibited localised degradation.

Displacement measurements recorded by the auxiliary LVDT reveal variations associated with the testing machine. To account for this effect, a flexible base is introduced in the model, incorporating additional system deformability, as detailed in Section 4.3.

Subsequently, Figure 12 compares the hysteresis curves for both rigid and flexible base configurations alongside the experimental results. This comparison highlights stiffness variations in the solid components of the base of the BDSL system, thus justifying the inclusion of the flexible base in the model.

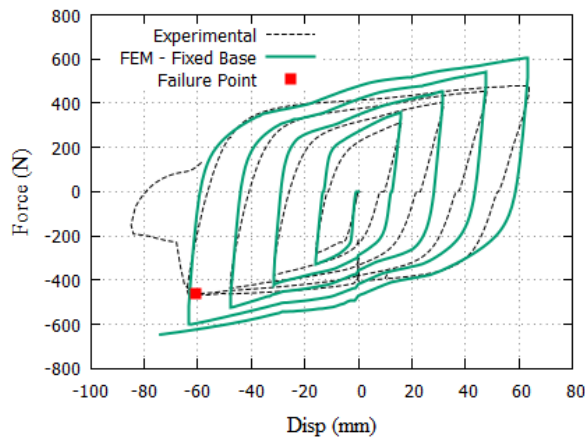


Figure 11. Hysteretic curves. Fixed-base dissipator and experimental result

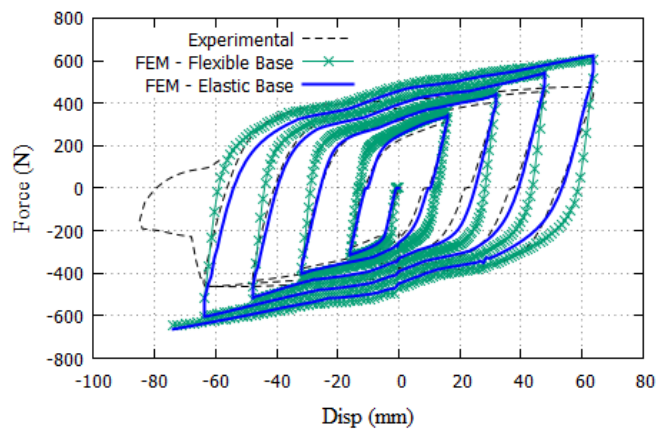


Figure 12. Hysteretic Curves. Fixed, flexible base cases and experimental results



#### 4.6 Mesh convergence study

This section explores the correlation between simulations and test results, focusing on the force-displacement response through a representative hysteretic curve. It also assesses the energy dissipated in each calibrated case, alongside the evolution of stiffness, effective strength, and equivalent viscous damping of the BDSL system. The analysis includes data from the three experimental configurations, highlighting variations and characteristic patterns in the dynamic response parameters.

A mesh convergence study was carried out to ensure numerical accuracy and stability. A BDSL device and its flexible base are created using three different mesh densities, as illustrated in Figure 13: Mesh1 had 1556 hexahedra, Mesh2 had 2904, and Mesh3 had 23280.

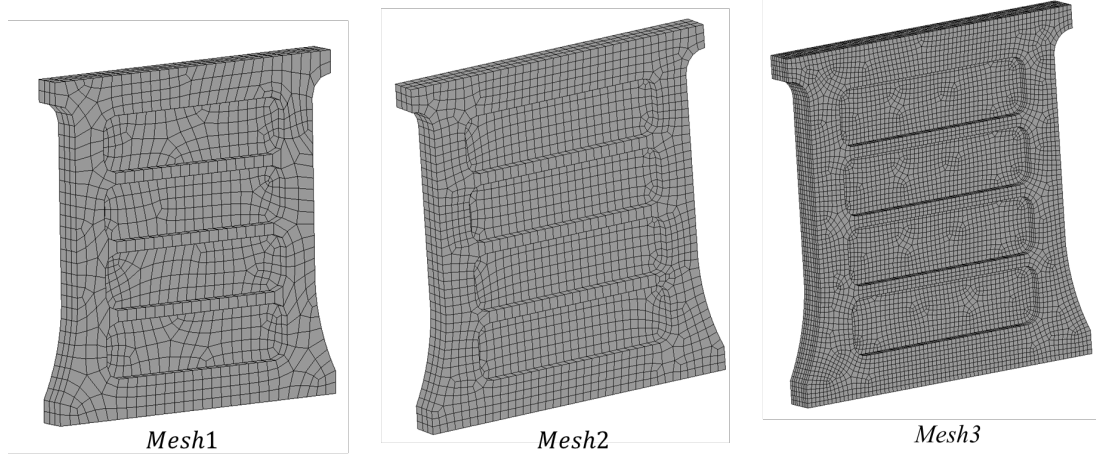


Figure 13. Mesh Discretization of the BDSL System

Figure 14 illustrates the hysteretic responses from the three mesh densities in comparison to the test N2 results. As the mesh is refined from mesh1 to mesh3, the numerical curves show improved agreement with the experimental data. For test N2, runtimes on a 16-core computer were approximately 2 hours 17 minutes for the coarse mesh, 4 hours 53 minutes for the medium, and 44 hours for the most refined.

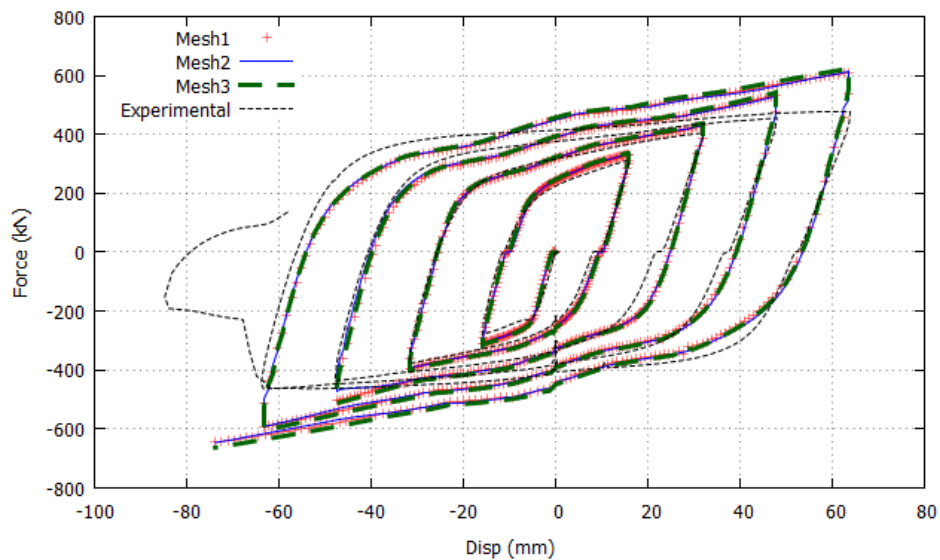


Figure 14. Hysteretic curves of meshes BDSL system

## 5 EXPERIMENTAL – NUMERICAL VALIDATION

### 5.1 Hysteretic curves

Figure 15 depicts the hysteretic response of specimens N1, N2, and N3 by comparing experimental data to finite element simulations. A satisfactory agreement is achieved between both responses. Distinct differences in the loading and unloading patterns can be observed, particularly in the larger cycles, reflecting the influence of the applied loading protocols and supporting the calibration of the numerical model.

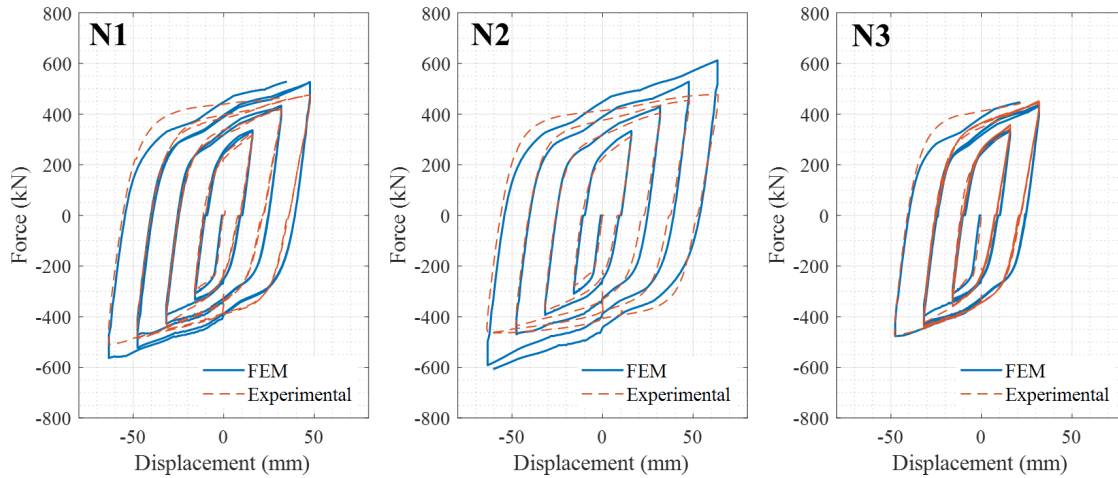


Figure 15. FEM calibration through hysteretic response comparison

### 5.2 Energy dissipation capacity

The energy absorbed by the BDSL system corresponds to the area enclosed by the hysteretic loops. Figure 16 presents the cumulative dissipated energy as a function of cumulative displacement for tests N1 to N3, comparing experimental data with FEM simulations. A close agreement is observed between the two, with slight differences in the energy accumulation trends, particularly for specimens N1 and N2.

As expected, the total energy dissipated per cycle increases with the applied displacement. Consequently, the cumulative energy continues to rise as the material undergoes further deformation. The final accumulated energy ranges from 240 to 310 kN·m, with slightly lower values recorded in the experimental tests compared to the numerical predictions.

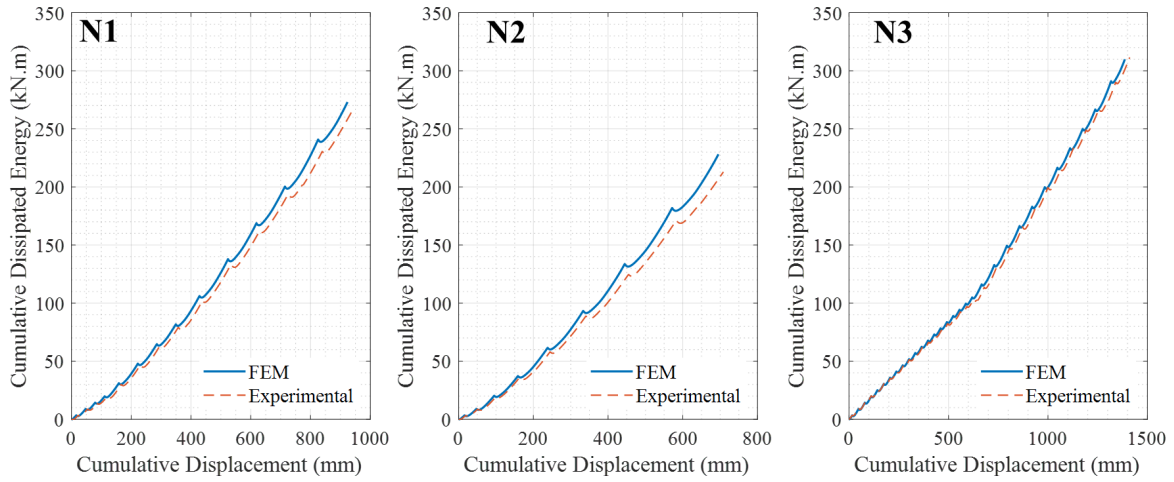


Figure 16. Comparison of cumulative energy dissipation between FEM and experiments

### 5.3 Stiffness Degradation and Effective Stiffness

Figure 17 presents the evolution of the secant stiffness obtained from the experimental tests and the calibrated FEM models. The degradation of secant stiffness is associated with the initiation and propagation of cracks, as well as the onset of plastic deformation in the steel, which together reflect the seismic performance of the BDSL device. This degradation can be estimated using the following expression:

$$\kappa_i = \frac{|F_i|}{|X_i|} \quad (1)$$

where  $F_i$  denotes the load, while  $X_i$  represents the displacement at the  $i$ -th peak [29]. A progressive degradation of stiffness is observed with increasing displacement, consistent with typical behaviour under cyclic loading. The FEM models do a good job of showing this trend, but there are some small differences where key points A (experimental) and B (numerical) are located, which are where different levels of structural damage are measured.

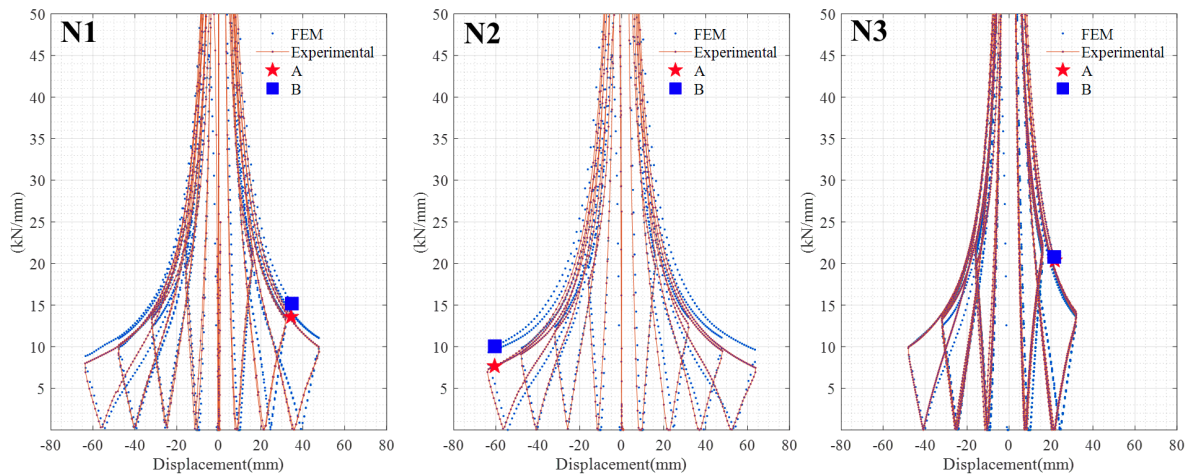


Figure 17. Comparison of stiffness degradation curves: FEM and experiments.

An analysis of structural response using linear dynamic analysis requires the definition of effective stiffness. Figure 18 presents the evolution of effective stiffness as a function of displacement based on the experimental tests. The physical meaning of effective stiffness is defined by the following equation:

$$K_{eff} = \frac{|P^+| + |P^-|}{|\delta^+| + |\delta^-|} \quad (2)$$

where  $P$  denotes the force and  $\delta$  represents the displacement in each cycle [30]. A clear decreasing pattern is observed, indicating stiffness degradation as displacement increases. This behaviour is consistent with damage accumulation under cyclic loading and confirms the expected reduction in lateral stiffness as plastic deformations develop.

#### 5.4 Equivalent Viscous Damping Coefficient

In the context of damper devices, the equivalent damping ratio  $\xi_{eq}$  is a widely used parameter to quantify energy dissipation [31]. It is derived based on the assumption of an equivalent linear viscous system. The expression used to estimate  $\xi_{eq}$  is given by:

$$\xi_{eq} = \frac{1}{2\pi} \cdot \frac{E_d}{E_{sd}} \quad (3)$$

Where:  $E_d$  represents the measured energy dissipated by the hysteretic loops of devices, and  $E_{sd}$  denotes the energy stored in an equivalent elastic spring. Figure 19 presents the variation of the equivalent viscous damping coefficient as a function of displacement for the experimental tests of specimens N1, N2, and N3. As the displacement increases, the damping coefficient rises significantly, reflecting the growing energy dissipation capacity of the system.

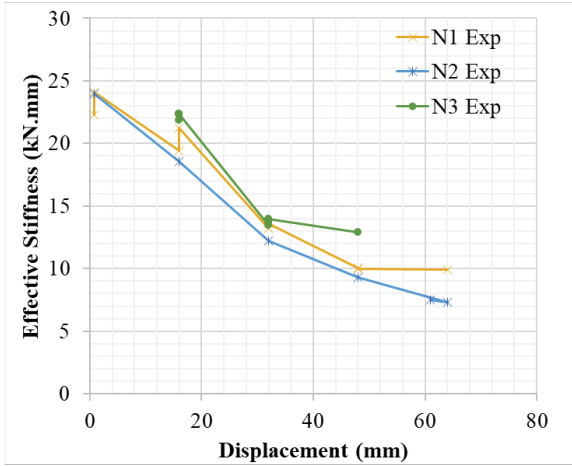


Figure 18. Effective stiffness vs displacement

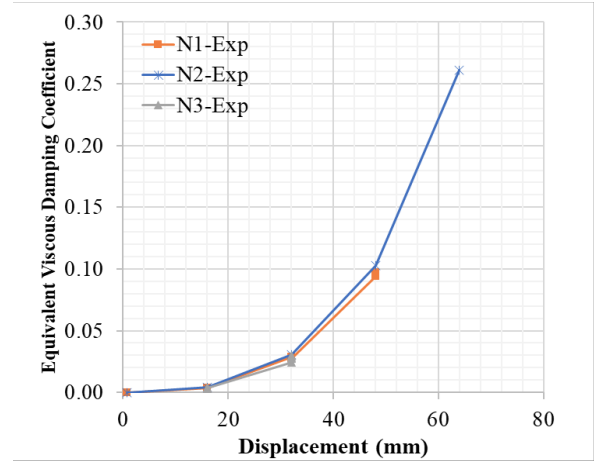


Figure 19. Equivalent viscous damping coefficient vs displacement

## 6 ANALYSIS OF RESULTS FROM THE FEM MODELS

This section presents key results obtained from the FEM simulations under cyclic loading and unloading of the BDSL system. The analysis includes the deformed shape, equivalent plastic strain distribution, TFD map, and observed failure modes for specimens N1, N2, and N3. To post-process the numerical simulations performed with COMPACK, the GiD postprocessor (Version 17.1.1.d) [32] was used.

Figure 20 presents the deformed shape in the Z-direction of the BDSL system for specimens N1, N2, and N3 under cyclic loading as obtained from FEM simulations. The contour plots represent the vertical displacement field, revealing local instabilities and buckling effects in specific areas of the device.

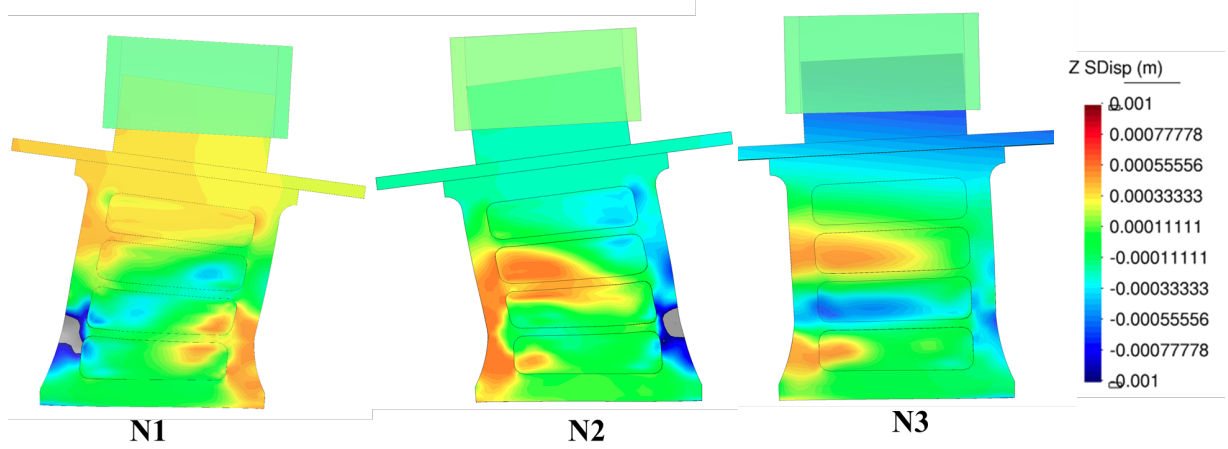


Figure 20. Deformed shape in Z-direction for specimens N1, N2, and N3 (FEM results).

In N1, a greater concentration of deformation is observed in the lower region, while N2 and N3 exhibit more distributed patterns, indicating differences in energy dissipation mechanisms due to the applied displacement histories, which include variations in the number of cycles and amplitude levels. Moreover, the buckling of the frame and the local buckling of the windows are effectively controlled by the presence of rigid vertical plates, which stabilise the system during cyclic response.

Following the analysis of the deformed shape, Figure 21 shows the equivalent plastic strain (EPS) distribution in tests N1, N2, and N3 obtained from FEM simulations under cyclic loading. The EPS field highlights the regions with the highest plastic demand, mainly concentrated around the horizontal windows and the lower corners of the device. These results confirm that the windows primarily work in shear while the frame is subjected to alternating tension and compression. As the displacement history becomes more severe, a progressive increase in plastic strain is observed, especially in N3, where the strain field becomes more uniform and reaches the highest levels. It can also be observed that once the frame starts to deteriorate, the overall response becomes unstable, which leads to distortion in the hysteretic curve and indicates structural damage.

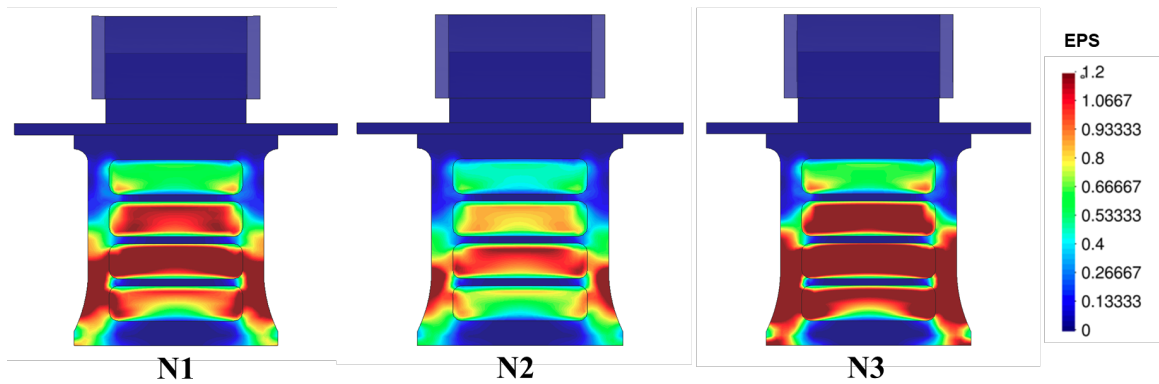


Figure 21. Plastic hardening in FEM Model

The Triaxial Failure Diagram (TFD) Map shown in Figure 23 corresponds to the dissipative energy element of the BDSL system for specimens N1, N2, and N3. This map is generated by COMPACK based on the failure curve defined in the input file (section 4.4) and provides a normalised measure of proximity to material failure under cyclic loading. As the number of cycles and the displacement amplitude increase, the TFD values rise accordingly, which is also influenced by the large deformations induced by high-amplitude loading cycles.



In specimen N3, extensive regions reach values close to the maximum threshold, indicating a critical condition. These results confirm that energy dissipation is concentrated in the shear zones and that material degradation becomes more severe in the advanced stages of loading.

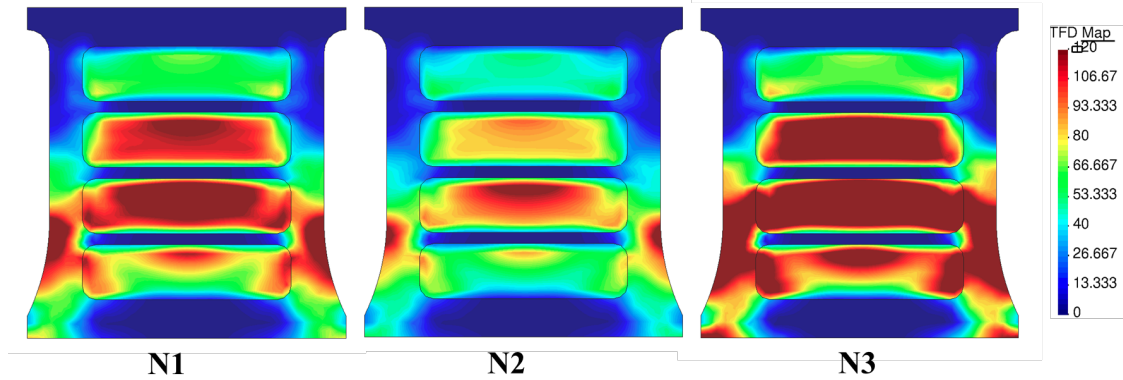


Figure 23. TFD Map of the dissipative element in the BDSL system.

To validate the previous observations, a post-processing analysis was carried out on the linear equivalent plastic strain and triaxiality at all nodes of the FEM model. Since the geometry remains constant, a representative case with an intermediate mesh density was selected. This configuration includes 1,076 structured mesh nodes in the dissipative window zones and 2,756 nodes in the surrounding frame.

Figure 24 shows the distribution of triaxiality versus linear equivalent plastic strain for frame points and window points in specimens N1, N2, and N3, together with the failure curve (TFC). The window zones (in orange) concentrate most of the plastic demand, with many points approaching or exceeding the TFC curve, particularly in specimen N3. In contrast, the frame points (in blue) exhibit a wider but lower spread of plastic strain. However, the strain values in the frame zone are globally higher, which suggests that a failure mechanism in the frame could lead to the collapse of the system, as observed in the full-scale experimental test.

As the cyclic loading progresses, more points enter critical regions defined by the TFC, indicating a growing risk of failure and confirming the role of the window zones as the primary energy dissipation areas.

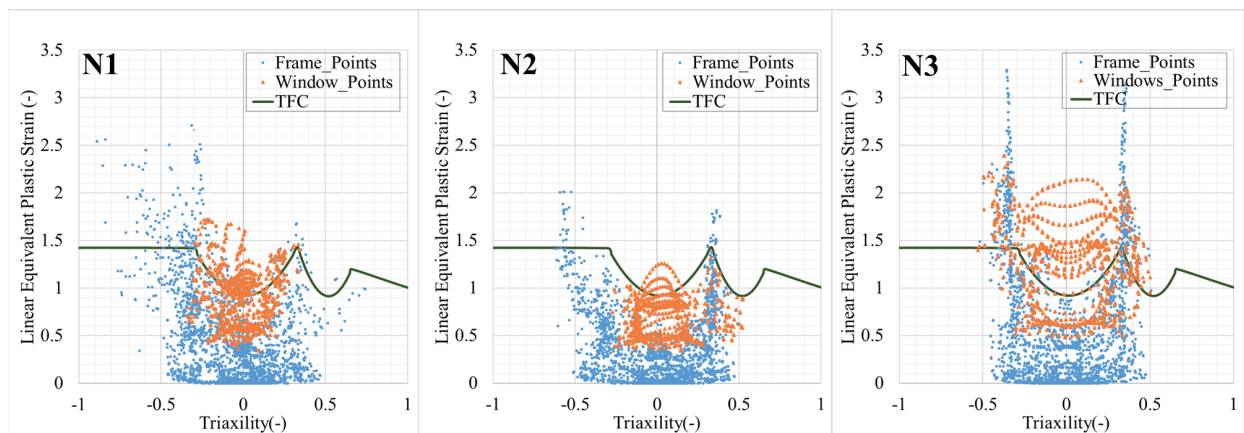


Figure 24. Triaxiality vs equivalent plastic strain compared to the TFC curve for specimens N1–N3.

Figure 25 shows the safety zone map based on the TFD criterion for specimens N1, N2, and N3, identifying different levels of structural demand. These zones allow for the assessment of the local material condition, ranging from compression to failure scenarios.



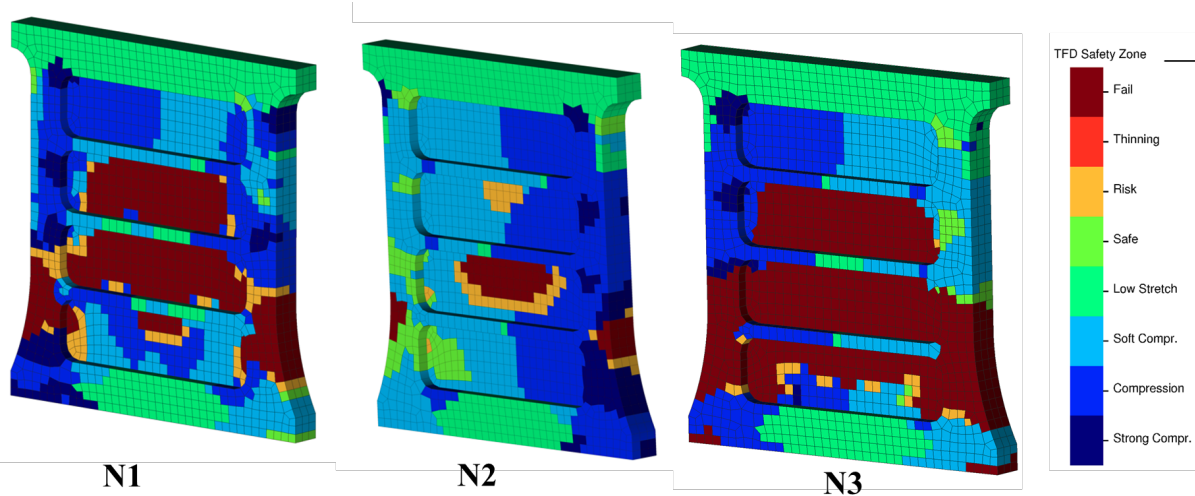


Figure 25. TFD Safety Zones for tests N1, N2, and N3

The results show that specimens N1 and N3 concentrate higher levels of damage in the window areas, reaching zones classified as risk or failure. In contrast, specimen N2 remains mostly in the safe zones, indicating less damage progression. However, the specimen from the N2 test was also subjected to high amplitudes, suggesting that the more stable response could be associated with a more controlled distribution of deformations. In all three cases, the frame fails at the lower part, indicating a common weak point in the geometry under cyclic loading.

In the case of N3, it is observed that the specimen undergoes many cycles of small amplitudes, which could lead to failure due to ultra-low cycle fatigue, given the extremely high number of loading cycles. This analysis reinforces the usefulness of the TFD as a tool for detecting critical regions under seismic demand.

Figure 26 shows the experimental and FEM failure modes for specimen N3. Panel (a) displays the TFD safety zone map from the FEM analysis, highlighting the different structural demand zones, ranging from safe to risk and failure areas. Panel (b) shows the experimental view of specimen N3, revealing the damage after testing, with visible deformation and material behaviour under load. Finally, panel (c) provides a close-up of the failure area, where the frame has suffered significant damage due to excessive deformation. This figure provides a clear comparison between the simulated and observed failure modes, demonstrating how the FEM analysis aligns with the experimental results.

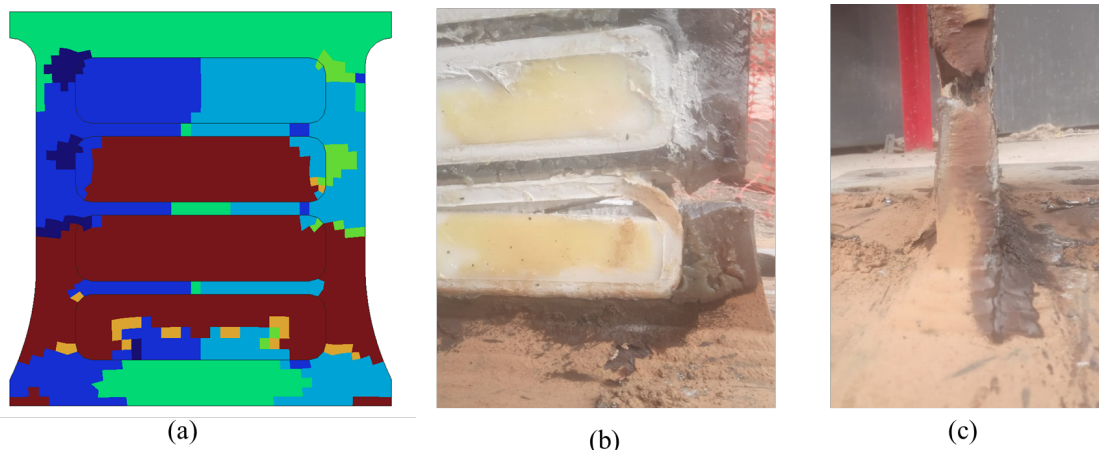


Figure 26. FEM and experimental failure mode for N3

## 7 MACHINE LEARNING-BASED SURROGATE MODEL

The results presented in the previous section clearly demonstrate the capabilities of the FEM model developed in this study. However, its high computational cost and the complexity involved in setting up the models pose significant limitations, particularly when analysing multiple configurations or requiring rapid results. In this context, Machine Learning (ML)-based surrogate models offer an efficient alternative to traditional numerical simulations by approximating complex physical phenomena with significantly reduced computational cost. These models leverage data-driven approaches to identify underlying patterns in high-dimensional datasets, enabling fast and accurate predictions of system behaviour.

In structural engineering, ML surrogate models play a crucial role in design optimization, model calibration, reliability assessments, and real-time decision-making [33]. Their ability to approximate computationally expensive simulations makes them valuable tools for evaluating and improving the performance of seismic response control devices [34 - 36], such as the Shear Link Bozzo (BDSL) system.

As an initial approach, we aim to determine whether ML-based surrogate models can accurately predict the hysteretic curve for different device configurations. In future work, this methodology will be extended to predict damage, further enhancing the applicability of ML techniques in the design improvement of these structural devices.

### 7.1 Data Preparation and Feature Selection

Developing a reliable ML-based surrogate model requires a sufficient amount of high-quality data. Since the current project is an initial study, experimental results were not considered at this stage, as they typically contain more noise, invalid data, and outliers. Instead, the dataset was built on the calibrated FEM layout presented in previous sections.

Specifically, we conducted 16 FEM simulations using the same device while varying the thickness of its windows. Each simulation involved 8 loading cycles of constant amplitude, with the amplitude varying between simulations. The thickness of the frame is considered constant and equal to 25 mm. Table 1 summarises the configurations of these 16 calculations. For model evaluation, data from 15 of the 16 simulations were used for training, while one was reserved for testing. In particular, Model 2 was selected as the test case, as highlighted in Table 2.

Table 2. Configuration of the 16 simulations used to evaluate the ML-based surrogate model.

Model 2, highlighted in gray, was used for validation.

Model	Window thickness [mm]	Cycle Amplitude [mm]	Model	Window thickness [mm]	Cycle Amplitude [mm]
1	6	8	9	10	8
2	6	16	10	10	16
3	6	32	11	10	32
4	6	48	12	10	48
5	8	8	13	12	8
6	8	16	14	12	16
7	8	32	15	12	32
8	8	48	16	12	48

The FEM simulations provide the force at each point of the hysteretic curve, establishing a relationship between actuator displacement and the force required to reach that displacement. For our ML model, the target variable is the force corresponding to each actuator

displacement at a given time. However, using only the instantaneous actuator displacement to train the model is insufficient, as the force depends not only on the current displacement but also on the device's deformation history. Therefore, additional input variables derived from the primary input (displacement) were included to provide the ML model with historical deformation information.

After a detailed analysis, the following key features were selected:

- Thickness of the window.
- Displacement at that instant.
- Loading cycle number (as an integer).
- Maximum amplitude of the cycle.
- Absolute cumulative displacement.
- Direction of the load at that instant.
- Force (output variable of the model).

## 7.2 Model Training and Validation

The surrogate model was developed using supervised learning techniques, specifically regression, as the target variable (force) is continuous. The primary model chosen was the Gradient Boosting Regressor (BRT), selected for its robust predictive capabilities and minimal sensitivity to hyperparameter tuning. BRT models construct a series of weak learners (typically shallow decision trees) in an iterative process, refining predictions by correcting errors from previous iterations. Given its reliability and strong predictive performance, BRT was chosen as the primary model [37]. However, future work will explore other ML models.

The model fitting and computations were performed using the *GradientBoostingRegressor* class from the *Scikit-Learn Python* library [38].

A key advantage of BRT, along with other tree-based methods such as Random Forests, is its ability to allocate a portion of the dataset for validation during training. This helps prevent overfitting and ensures that the model generalizes well to unseen data. The internal validation fraction also enables automatic early stopping, reducing unnecessary computations. Since BRT sequentially builds weak learners, model accuracy is monitored at each iteration using the validation set. If performance does not improve over a predefined number of consecutive iterations, training is halted to prevent overfitting and excessive computation.

For this study, we imposed the following hyperparameters:

- Maximum number of trees (*n\_estimators*): 10000
- Validation data fraction (*validation\_fraction*): 0.25
- Tolerance for consider improvement between iterations (*tol*): 1.0
- Number of iterations without change for early stopping (*n\_iter\_no\_change*): 100

Applying these hyperparameters, we trained the model with data from the 15 simulations in Table 2 and tested its ability to predict the hysteretic curve of Model 2. The Mean Absolute Error (MAE) of the predictions was 13.55 kN, which is reasonable given that the force ranges from -400 kN to 400 kN.

Figure 24 shows the actual vs. predicted hysteretic curve for Model 2. The differences between the two curves are minimal, indicating that the model provides accurate predictions.

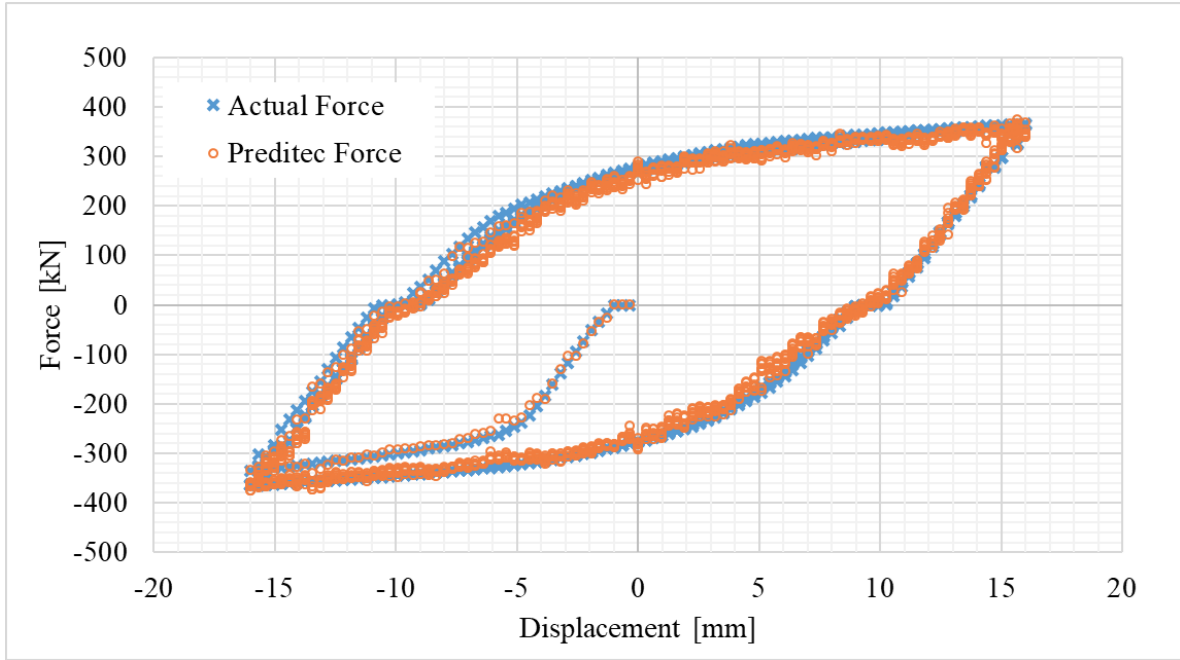


Figure 27. Comparison of the hysteretic curve obtained from FEM simulations and the ML-based surrogate model.

### 7.3 Predictive Capabilities and Optimization Potential

The results demonstrate the potential of ML-based surrogate models in structural engineering. The entire training and testing process took approximately three minutes on a standard PC, whereas performing the same calculations using the FEM required 16 hours to simulate 10 cycles.

While the results presented here are not disruptive, they highlight the promising capabilities of ML-based surrogate models. Future improvements will involve incorporating additional geometric parameters, such as varying thicknesses for different windows, and extending the model to predict damage. This will require further FEM simulations for training, but once trained, the model will allow rapid evaluation of thousands—or even millions—of configurations in a reasonable time frame.

## 8 CONCLUSIONS

- This research enabled an accurate representation of the BDSL device's behaviour under cyclic loads and led to a numerical–experimental methodology to characterise its structural response.
- A numerical model based on the FEM is built, including proper boundary conditions, contact surfaces, a constitutive model, nonlinear formulations, and a triaxial failure curve to reproduce the dissipation response.
- The numerical results were compared to the experimental results after the constitutive parameters were calibrated. The results showed a good agreement in both the hysteretic curves and the specific parameters of the device, such as how much energy was lost and how stiff the material became over time.
- The numerical models ensure a comprehensive and accurate representation; considering the nonlinear behaviour of the materials in the simulations, they allow for a physical response. Incorporating precise mechanical contact parameters portrays the complex interactions of components in the structure.

- Numerical simulation data has been used to develop a machine learning-based surrogate model. After validation, the model provides excellent approximations in significantly less time. These techniques offer potential future applications by combining autonomous learning models with both synthetic and experimental data.
- Finally, parameter calibration guarantees a close alignment with physical laboratory testing. The numerical model demonstrated its ability to reproduce the behaviour observed with the device.

## 9 ACKNOWLEDGEMENTS

The authors acknowledge the financial support of the *Projecte ACE100/23/000022 – Edificacions resilientes equipades amb dissipadors Shear Link*, funded by the Government of Catalonia through ACCIÓ and with the support of the Catalan Office for Climate Change, with the participation of Luis Bozzo Estructuras y Proyectos S.L. and the *Centre Internacional en Mètodes Numèrics a l'Enginyeria (CIMNE)*.

## REFERENCES

- [1] Bozzo, L. M., & Barbat, A. H. (1999). Diseño sismorresistente de edificios - Técnicas convencionales y avanzadas. Barcelona: REVERTE.
- [2] Soong, T.T. and Spencer, B.F. (2002). Supplemental energy dissipation: state-of-the-art and state-of-the practice. *Engineering Structures*, 24, pp.243–259.
- [3] Symans, Charney, Whittaker, Constantinou, Kircher, Johnson and Mcnamara, R.J. (2008). Energy Dissipation Systems for Seismic Applications: Current Practice and Recent Developments. *ASCE Journal of Structural Engineering*, 2008.
- [4] Popov, E. P., Kasai, K., & Engelhardt, M. (1987). Advances in design of eccentrically braced frames. *Bulletin of the New Zealand National Society for Earthquake Engineering*
- [5] Hurtado, F. and Bozzo, L.M. (2008). Numerical and experimental analysis of a shear-link energy dissipator for seismic protection of buildings. *14th World Conference on Earthquake Engineering*, 2008.
- [6] Nuzzo, I., Losanno, D., Caterino, N., Serino, G. and Bozzo Rotondo, L.M. (2018). Experimental and analytical characterization of steel shear links for seismic energy dissipation. *Engineering Structures*, 172, pp.405 418.
- [7] Bozzo, G. (2021). Una nueva generación de disipadores SLB “Shear Link” para el diseño sismorresistente. *Universidad Politécnica de Cataluña*.
- [8] Bozzo Rotondo et al., "Buckling Delayed Shear Link" U.S. Patent Application 17/967,199, United States Patent and Trademark Office, 2024
- [9] Bozzo, L.M., Gonzales, H., Pantoja Medina, M., Muñoz, E. and Ramirez, J. (2019). Modeling, analysis and seismic design of structures using energy dissipators SLB. *International Symposium on Earthquake Engineering*, 2019.
- [10] Bozzo, L. M., Ramirez, J., Bairan, J., Bozzo, G., & Muñoz, E. (2020). Precast buildings equipped with SLB seismic devices. In the *17th World Conference on Earthquake Engineering*.
- [11] Ramírez Machado, B. J. (2020). Estudio comparativo para edificación de 5 plantas empleando solución prefabricada y disipadores SLB y solución convencional en zona de sismicidad alta de Perú (Master's thesis, Universitat Politècnica de Catalunya).
- [12] Illarregui, N. (2021). Disipación de energía sísmica en puentes de luces continuas. *Universidad Politécnica de Cataluña*.

- [13] Bozzo Fernández, Guillermo, et al. "Optimal set-up configuration for testing stiff energy-dissipating devices under large displacements." WCEE 18: World Conference on Earthquake Engineering: online proceedings. International Association for Earthquake Engineering, 2024
- [14] Ramirez, J., et al. "ADVANCES IN THE DESIGN OF ENERGY DISSIPATING DEVICES. EXPERIMENTAL AND NUMERICAL CHARACTERIZATION."
- [15] ANSI/AISC 341-16, «Seismic Provisions for Structural Steel Buildings,» American Institute of Steel Construction, Chicago, 2016.
- [16] ASCE (2021)– ASCE/SEI 7-22 Standard: Minimum Design Loads and Associated Criteria for Buildings and Other Structures (American Society of Civil Engineers (ASCE)).
- [17] Rastellini, F., Oller, S., Salomón, O., & Oñate, E. (2008). Composite materials non-linear modelling for long fibre-reinforced laminates: Continuum basis, computational aspects and validations. *Computers & structures*, 86(9), 879-896.
- [18] Martinez, X., Oller, S., Rastellini, F., & Barbat, A. (2008). A numerical procedure simulating RC structures reinforced with FRP using the serial/parallel mixing theory. *Computers and Structures*, 86(15–16), 1604-1618.
- [19] Flores, F. G. (2001). Elementos finitos para el análisis de sólidos anisótropos con grandes deformaciones plásticas. *Mecánica Computacional*, (5), 171-178.
- [20] Yoshida, F., & Uemori, T. (2002). A model of large-strain cyclic plasticity describing the Bauschinger effect and workhardening stagnation. *International journal of plasticity*, 18(5-6), 661-686.
- [21] Yoshida, F., Uemori, T., & Fujiwara, K. (2002). Elastic–plastic behavior of steel sheets under in-plane cyclic tension–compression at large strain. *International journal of plasticity*, 18(5-6), 633-659.
- [22] Yoshida, F., & Uemori, T. (2003). A model of large-strain cyclic plasticity and its application to springback simulation. *International Journal of Mechanical Sciences*, 45(10), 1687-1702.
- [23] Jia, Liang-Jiu, and Hitoshi Kuwamura. "Prediction of cyclic behaviors of mild steel at large plastic strain using coupon test results." *Journal of Structural Engineering* 140.2 (2014): 04013056.
- [24] Agelet de Saracibar, C. (1990). *Finite Element Analysis of Sheet Forming Processes*. Universitat Politècnica de Catalunya, Barcelona, Spain.
- [25] Zhong, Z. (1993). *Finite Element Procedures for Contact Impact Problems*. Oxford Univ. Press.
- [26] Flores, F. G. (2000). Un algoritmo de contacto para el análisis explícito de procesos de embutición. *Revista internacional de métodos numéricos*.
- [27] Rastellini, F., Socorro, G., Forgas, A., & Onate, E. (2016, August). A triaxial failure diagram to predict the forming limit of 3D sheet metal parts subjected to multiaxial stresses. *Journal of Physics: Conference Series*, 734(3), 032020.
- [28] Zhuang, Chenxu, et al. "Ductile fracture characterization of A36 steel and comparative study of phenomenological models." *Journal of Materials in Civil Engineering* 33.1 (2021): 04020421.
- [29] Yang, Y., Gao, S., Zheng, Y., Liu, X., Zhang, W., & Lin, B. Q. (2023). Seismic performance of precast column-beam joint with artificial plastic hinge. *Journal of Building Engineering*, 67, 105942.
- [30] Teruna, Daniel R., Taksiah A. Majid, and Bambang Budiono. "Experimental study of hysteretic steel damper for energy dissipation capacity." *Advances in Civil Engineering* 2015.1 (2015): 631726.



- [31] Chopra, A. K. (1995). Dynamics of Structures. Prentice Hall. Inc. USA, 729.C.
- [32] GiD: The personal pre and postprocessor, International Center for Numerical Methods in Engineering (CIMNE). URL: /www.gidhome.com
- [33] Irazábal, J., Salazar, F., & Vicente, D. J. (2023). A methodology for calibrating parameters in discrete element models based on machine learning surrogates. Computational Particle Mechanics, 10(5), 1031-1047.
- [34] Hu, S., Wang, W., & Lu, Y. (2023). Explainable machine learning models for probabilistic buckling stress prediction of steel shear panel dampers. Engineering Structures, 288, 116235.
- [35] Bae, J., Lee, C. H., Park, M., Alemanyeh, R. W., Ryu, J., & Ju, Y. K. (2020). Modified low-cycle fatigue estimation using machine learning for radius-cut coke-shaped metallic damper subjected to cyclic loading. International Journal of Steel Structures, 20, 1849-1858.
- [36] Hu, Y., Guo, W., Long, Y., & Li, S. (2022). Physics-informed deep neural networks for simulating S-shaped steel dampers. Computers & Structures, 267, 106798.
- [37] Friedman, J. H. (2001). Greedy function approximation: a gradient boosting machine. Annals of statistics, 1189-1232.
- [38] Pedregosa, F., Varoquaux, G., Gramfort, A., Michel, V., Thirion, B., Grisel, O., ... & Duchesnay, É. (2011). Scikit-learn: Machine learning in Python. Journal of Machine Learning Research, 12, 2825-2830.